



## PAPER

## OPEN ACCESS

## RECEIVED

27 September 2025

## REVISED

16 December 2025

## ACCEPTED FOR PUBLICATION

5 January 2026

## PUBLISHED

20 January 2026

Original content from this work may be used under the terms of the [Creative Commons Attribution 4.0 licence](#).

Any further distribution of this work must maintain attribution to the author(s) and the title of the work, journal citation and DOI.



# Negative charge acquisition by isolated single microdroplets from plasma exposure at atmospheric pressure

Nourhan E Hendawy<sup>1,2,\*</sup> , Harold N McQuaid<sup>3,\*</sup> , Somhairle Mag Uidhir<sup>3</sup>, David Rutherford<sup>4</sup>, Declan Diver<sup>5</sup> , Davide Mariotti<sup>6</sup>  and Paul Maguire<sup>5,\*</sup>

<sup>1</sup> School of Life Sciences, Sussex University, Brighton, United Kingdom

<sup>2</sup> Biaco Energy Ltd, Hassocks, United Kingdom

<sup>3</sup> School of Engineering, Ulster University, Belfast, United Kingdom

<sup>4</sup> Faculty of Electrical Engineering, Czech Technical University, Technická 2, Prague 6, Czech Republic

<sup>5</sup> School of Physics and Astronomy, University of Glasgow, Glasgow, United Kingdom

<sup>6</sup> Faculty of Engineering, University of Strathclyde, Glasgow, United Kingdom

\* Authors to whom any correspondence should be addressed.

E-mail: [nourhan.hendawy@biaco.energy](mailto:nourhan.hendawy@biaco.energy), [h.mcquaid@ulster.ac.uk](mailto:h.mcquaid@ulster.ac.uk) and [paul.maguire@glasgow.ac.uk](mailto:paul.maguire@glasgow.ac.uk)

**Keywords:** atmospheric pressure plasma, plasma–liquid interaction, microdroplet charging, charge measurement, charged droplets, finite element simulations

## Abstract

Charged liquid microdroplets have generated significant interest recently due to the observation of chemical reaction rate enhancement by orders of magnitude. Droplet charging by plasma irradiation has been observed along with significantly enhanced reaction rates in liquid. In this paper, we measure the charge on fixed size ( $47\ \mu\text{m}$ ) individual droplets, exposed for approximately 4 ms to a low temperature RF-driven plasma operated at atmospheric pressure. The measured charge values ranged from  $2.5$  to  $3.5 \times 10^6$  electrons, depending on the droplet trajectory. Results were compared with finite element simulations of plasma charging, which provided estimates of surface electric fields and charge fluxes at the droplet surface and helped advance the development of a theoretical framework for plasma-charged microreactors.

## 1. Introduction

Interest in charged microdroplets has recently received considerable attention. Their unique chemical reaction environment offers increasing significance in many scientific and technological fields, from materials and drug synthesis to biological medicine [1–6]. Greatly enhanced chemical reaction rates, by many orders of magnitude, which occur in droplets within a specific size range have generated widespread interest in precision chemical synthesis [1, 7–9]. Reaction barriers that are extremely challenging in bulk liquids have been overcome, possibly due to high surface electric fields, with important climate-related consequences for high-energy industrial processes such as ammonia production and  $\text{CO}_2$  transformation [1, 3, 10–13]. Microdroplets have also been found to spontaneously induce redox reactions, with implications for chemical processes including those in living systems, such as photosynthesis and respiration [14–16].

The high surface-to-volume ratio and the effects of partial solvation on reaction rates are potentially important, as well as the suspected presence of surface charge and electric fields, which can lead to effects such as ultrathin electronic double layers; ion separation, confinement and alignment; enhanced concentration gradients and diffusive flows; extreme pH conditions, charge transport, and spontaneous redox reactions [5, 9, 17]. Induced ionisation of gas and vapour molecules, droplet fission and plasma formation have also been postulated as a consequence of surface fields. However, charge levels and field intensities are unknown, with various alternative electrification and charge transfer mechanisms suggested [4, 7, 8, 13, 15, 17–19].

Microdroplets are a complex physiochemical system with multiple transient parameters that are difficult to control or measure experimentally. Observed effects are critically dependent on size, with an

upper limit of approximately 15  $\mu\text{m}$  diameter and a lower limit of a few microns, determined by lifetime and technical limits. Acquired surface charge is subject to recombination with gas-phase ions during flight. Droplet size and hence internal conditions evolve during flight, due to evaporation, fission and collisions, limiting experimental exposure typically to the sub-millisecond range. Electric fields, concentration gradients, solvent alignment and charge transfer are sensitive to size through their dependence on surface curvature and surface area to volume ratio. Thus, the development of a comprehensive theoretical framework is needed to fully exploit microdroplet capabilities.

Microdroplet charging by plasma offers an alternative or complementary approach that could allow greater elucidation of fundamental characteristics as well as enhanced technological capability. Upon entry into a low-temperature non-equilibrium plasma region, the high electron temperature ensures an initial net flux of high mobility free electrons from the gas phase to the droplet surface, creating a layer of surface charge and an associated electric field [20]. After the droplet floating potential is established, over a few nanoseconds, the electron and positive ion flux are equalized. Thereafter, the electrical characteristics remain reasonably constant over a known and controllable time period determined by plasma length and droplet velocity, assuming a uniform plasma density and temperature. A suitable plasma is required to operate at atmospheric pressure with low gas temperature to limit droplet evaporation and hence a relatively high gas flow and restricted plasma size is inevitable, presenting a challenge for injection of microscale droplets and charge measurement [21, 22]. We recently reported charge measurements on injected microdroplets into a similar RF-driven plasma as used here [23]. A stream of droplets of varying size and velocity was used and the average charge determined. Also, an extremely high rate of in-droplet  $\text{H}_2\text{O}_2$  synthesis was observed, demonstrating the remarkable microreactor capabilities of such droplets. In this paper, we measure the charge on single isolated droplets, of fixed size, in an enclosed flow capillary, using an exterior coaxial ring electrode, for which an electrostatic model was developed. Droplet trajectory, screening and neutralisation were also investigated and the resultant charge values compared to finite element simulation of charging fluxes within the plasma, based on a fully hydrodynamic drift-diffusion model.

## 2. Experimental

Individual microdroplets were generated at a rate of 20 Hz via a MicroFab (MJ-ATP-01) dispenser, which is a droplet-on-demand piezoelectric generator with an orifice diameter of 20  $\mu\text{m}$ , leading to an average microdroplet diameter of 47  $\mu\text{m}$ . They were injected into an RF-driven (13.56 MHz) atmospheric pressure plasma via a 2 mm (ID) quartz capillary tube, interfaced with a gas mixing manifold to allow injection of the plasma gas with limited turbulence. The droplets exit the Microfab orifice, typically at a velocity of a few  $\text{ms}^{-1}$ , into a 2 mm (ID) quartz capillary where they are carefully mixed with a plasma gas flow. After travelling a distance that allows the droplet velocity to equilibrate with that of the gas, the gas-droplet fluid system is expected to be laminar with a low Reynolds number. The droplet then passes through the plasma region and onto the ring electrode region. The dispenser injection angle is adjusted manually to position the droplet stream in the centre of the capillary, in one axis. However, visual access to the other axis is not available and hence the droplet stream may be offset a distance  $x$  from the radial centre of the second axis, and  $x$  may vary with distance along the capillary. Gas and droplet velocities were measured separately, within the plasma region, and assuming that the gas flow is laminar and therefore has a parabolic velocity profile, we can estimate the value of  $x$  offset with the assumption that Stoke's regime (low Reynolds number  $\sim 0.8$ ) pertains and that the two velocities are equal. From Stoke's law, the droplet distance travelled to reach terminal velocity was calculated to be 2.2 mm, while the distance between gas inlet and plasma is  $>10$  mm, therefore the assumption of equal velocities is reasonable.

The low temperature plasma was generated between two exterior concentric Cu electrodes,  $\sim 2$  mm apart and operated in He gas with controlled input gas flows from 0.7 to 1.3 sLm, figure 1. The acquired charge on the microdroplet, due to plasma exposure, was detected using a thin coaxial ring electrode, located outside the capillary and downstream from the plasma, which was surrounded by a Faraday shield to minimize RF induced noise. The current pulse signal was amplified via a low noise charge amplifier (Amptek A250F, A250) and captured on an oscilloscope (Tektronix MDO34). Electron density was estimated from *in-situ* RF impedance measurements (Impedans Octiv Suite 2.0) using an electron mobility model, assuming a uniform coaxial plasma between electrodes [24].

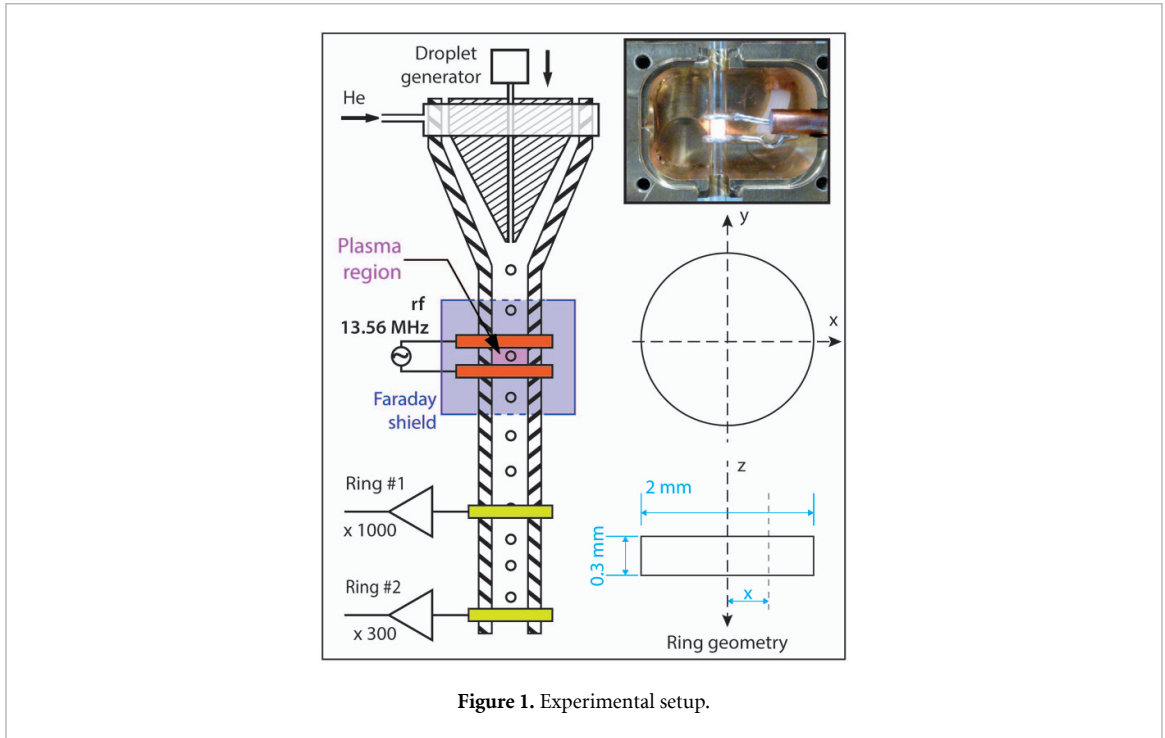


Figure 1. Experimental setup.

### 3. Theory

The induced current is determined using Ramo—Shockley theorem by assuming the ring electrode of radius  $a$  and length  $w$ , with  $w \ll a$ , as a series of slices [25–27]. For a charged droplet travelling, with velocity  $v$ , through a ring electrode, at an offset  $x$  from the radial centre, then the distance,  $R$ , between the droplet centre at coordinate  $(x, 0, z_d(t))$ , where  $z_d(t) = vt$ , and point  $z$  on the ring, at coordinate  $(a \cos \theta, a \sin \theta, z)$ , is given by

$$R(x, z, z_d, \theta) = \sqrt{(z - vt)^2 + x^2 + a^2 - 2ax \cos \theta}. \quad (1)$$

Ignoring the  $\cos \theta$  term would allow a simple derivation of closed form expressions for induced charge,  $Q_i(t)$ , and current,  $I(t)$ . However, for offset values  $x > 0.6a$ , this leads to significant errors. The induced current on the ring electrode is given by

$$I(t) = -\varepsilon_0 \frac{d\varphi(t)}{dt} \quad (2)$$

where

$$\varphi(t) = \int_{-w/2}^{w/2} \int_0^{2\pi} E_n(\theta, z, t) a \, d\theta \, dz. \quad (3)$$

Is the outward normal flux through the cylindrical surface and  $E_n$  is the normal component of electric field at the wall, given by

$$E_n(\theta, z, t) = \mathbf{E} \cdot \mathbf{e}_r = \frac{Q}{4\pi \varepsilon_0} \frac{a - x \cos \theta}{[a^2 + x^2 - 2ax \cos \theta + (z - vt)^2]^{3/2}}. \quad (4)$$

By differentiating to get  $\partial E_n / \partial t$ , the expression for current is

$$I(t) = -\frac{3Qva}{4\pi} \int_{-w/2}^{w/2} \int_0^{2\pi} \frac{(a - x \cos \theta)(z - vt)}{[a^2 + x^2 - 2ax \cos \theta + (z - vt)^2]^{5/2}} \, d\theta \, dz. \quad (5)$$

The double integral is numerically evaluated in MATLAB with a specified absolute error tolerance and relative error tolerance of  $10^{-10}$  and  $10^{-6}$  respectively.

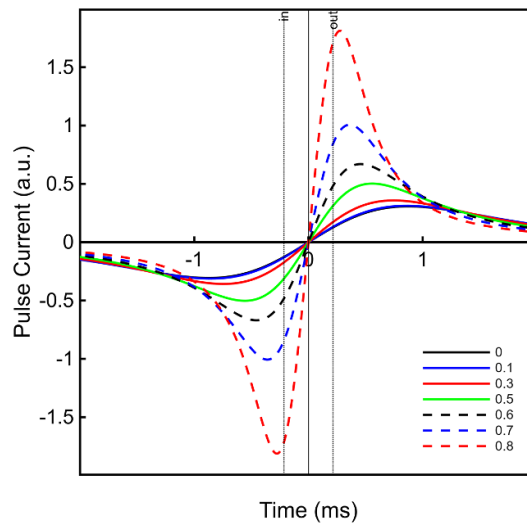


**Figure 2.** Variation in pulse width and amplitude for various axial offset values,  $x$ , from 0 up to  $0.8a$ , where  $a$  is the radius of the capillary.

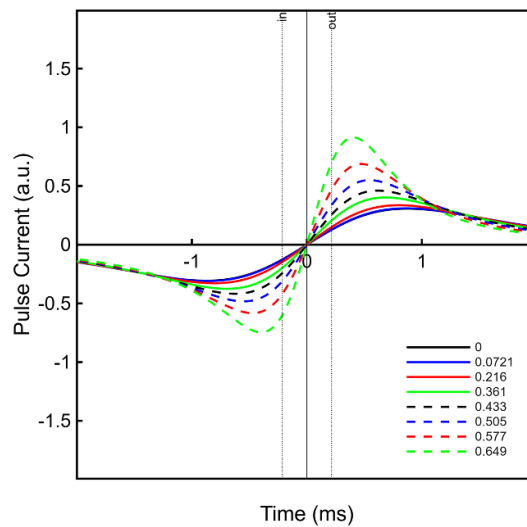


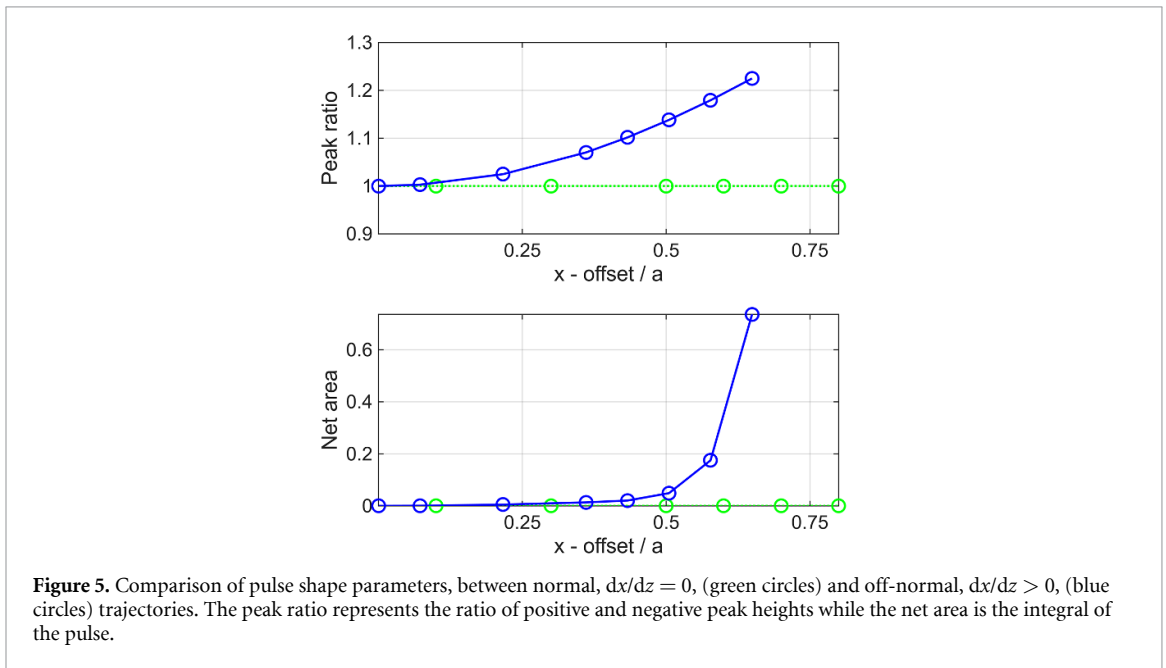
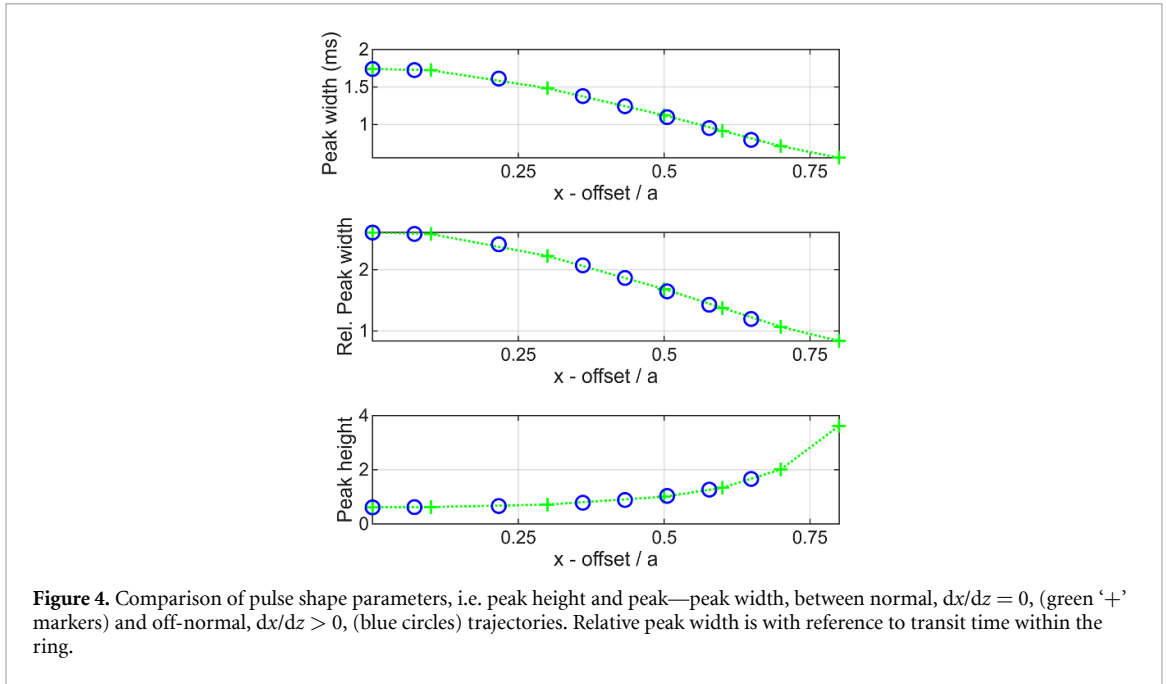
**Figure 3.** Variation in pulse width and amplitude for various droplet trajectories where  $dx/dz > 0$ , for various entry axial offset values,  $x$ , from 0 up to  $0.65a$ , where  $a$  is the radius of the capillary.

Ideally, the pulse amplitude is dependent on one unknown,  $Q$ , provided the droplet velocity is known. However, the ring response becomes sensitive to the axial offset,  $x$ , once the droplet is sufficiently close to the wall, figure 2. Furthermore, for droplet trajectories where  $dx/dz > 0$ , pulse asymmetry is introduced, figure 3.

A comparison of the pulse height and peak—peak width between a fixed axial trajectory, normal to the ring axis, and one that drifts off-normal, is given in figure 4, indicating a close similarity. As the offset value increases, beyond  $x/a > 0.5$ , the peak height increases while the pulse also narrows.

The off-normal trajectory gives rise to an asymmetrical pulse where, for  $x/a > 0.5$  and increasing within the ring, figure 5, the negative peak amplitude is reduced compared to the positive, while the integrated area under the pulse becomes increasingly positive.

The microdroplet velocity is determined from imaging in one plane ( $y$ -axis) before and after the plasma region. It is also calculated from the time delay between pulses using a pair of ring electrodes. Simultaneous imaging in the second plane ( $x$ -axis) is not possible. Therefore, any  $x$ -offset value is estimated by comparing the observed velocity to that expected from the gas velocity, assuming laminar flow conditions and that the droplet velocity has equilibrated to that of the gas. Gas velocity under laminar



flow conditions can generally be determined from the upstream set flow values. However, the mixing manifold is designed to minimise back pressure and turbulence while also allowing manual adjustment of the droplet trajectory. As a consequence, capillary gas flow downstream of the manifold is less than the set flow and is therefore measured downstream via liquid displacement tests. In the experimental set flow of 0.7 sLm, the capillary flow value was measured at 0.4 sLm.

The impact of the plasma environment on the ring electrical response also needs to be considered. Beyond the plasma electrodes, a plasma afterglow region is expected where the plasma density decays to zero over a distance  $L_{pa}$ . A ring electrode situated at a distance  $L_R$  from the nearest plasma electrode, where  $L_R < L_{pa}$ , will detect a reduced charge in the droplet due to Debye shielding. The effective charge measured is, to a first approximation, given by

$$Q_{\text{eff}} = Qe^{-\frac{s}{\lambda_D}} \tag{6}$$

where  $s$  is the distance between droplet and ring and  $\lambda_D$  is the Debye length, given by

$$\lambda_D = \sqrt{\frac{\epsilon_0 k T_e}{n e^2}}. \quad (7)$$

To minimise the Debye shielding effect on the measured charge requires  $s/\lambda_D \ll 1$ , i.e. the ring is placed beyond the afterglow region, where  $\lambda_D$  is much larger. While the precise extent of the afterglow is unclear, an approximation is obtained from the plasma luminance decay profile obtained under various plasma conditions. Current measurements, obtained from a microscale probe in direct contact with the plasma effluent, also provide an indication of the extent of the afterglow region where the current direction changes from negative (towards plasma) to positive. Beyond the afterglow, therefore, a region of low-density positive ion space charge is indicated, likely arising as a result of the net loss of more mobile electrons once outside the plasma. This background space charge will also result in screening of the droplet charge. The net charge visible on the ring is that of the droplet minus the total positive charge between the droplet and the ring. To a first approximation this is given by the term

$$Q_+ = n_+ A s \quad (8)$$

where  $A$  is the area of the capillary cross-section and  $n_+$  is the average ion density. This screening effect is expected to decrease on approach and reach a minimum when the droplet is within the ring. Another effect arises in that the presence of a background positive space charge will partially neutralise the droplet charge through ion recombination. Charge reduction due to transit through a space charge region has previously been considered as the swept charge, i.e.  $n_+ A s$  [28]. However, this assumes that the relative velocity between particle and space charge is significant, which is unlikely to be the case here. Instead, the random ion flux to the droplet surface is the dominant factor, such that the reduction in charge value per second is given by

$$e\Gamma A = e n_{\text{ion}} 4\pi R_d^2 \sqrt{\left(\frac{8k_B T_{\text{ion}}}{\pi m_{\text{ion}}}\right)} \quad (9)$$

where  $\Gamma$  is the ion flux,  $A$  the surface area and  $R_d$  the droplet radius. The magnitude of the charge reduction between plasma and ring is estimated using a value of  $n_+$  determined from the fit to the current pulse, from (8). The pulse amplitude on a second ring electrode also provides an estimate.

## 4. Results

To establish the optimal position for the ring, as close as possible to the plasma but outside the afterglow region, figure 6, the length of the afterglow was estimated electrically and from the luminance profile for various plasma power and flow conditions. The luminous length, in the absence of droplets, was observed to increase linearly with power, reaching 20 mm at 5 W but reduced to 10 mm at 5 W, on introduction of droplets, figure 7. The electrical response indicates a positive ion current flow (from the plasma) at low powers, with the appearance of electron current flow, i.e. a reduction in positive current, occurring above a threshold power value, which varies with distance. Ultimately, at high enough powers, the current is negative and indicates that the electrode is in full contact with the plasma afterglow. In figure 8, the effluent current versus power is shown for various plasma to electrode distances for plasmas without droplets, which confirms the luminance image conclusions. The ring electrode was therefore positioned at a distance of 10 mm from the nearest (ground) plasma electrode. A typical current pulse for a single droplet is shown in figure 9, with a peak positive voltage of  $\sim 150$  mV, equivalent to 150 pA. The time interval between the negative and positive pulse peaks is  $\sim 1$  ms.

Droplet size and velocity were determined from image measurements at the piezo tip and in the plasma region (without plasma ignited) for various generating and plasma conditions, figure 10. The observed droplet diameter was  $47 \mu\text{m} \pm 5\%$  at release from the piezo tip and remained constant beyond the ring, within the imaging resolution. For a plasma evaporation rate constant,  $c_{\text{evap}}$ , of  $3 \times 10^{-8} \text{ m}^2 \text{ s}^{-1}$ , previously determined for a similar plasma system, and assuming  $D_{\text{final}}^2 = D_0^2 c_{\text{evap}} t$ , the expected reduction is  $< 2 \mu\text{m}$  [22]. For a 20 Hz droplet stream, the observed average velocity was  $0.45 \pm 3\% \text{ m s}^{-1}$  in a measured gas flow of 0.4 sLm. In this flow scenario, the Reynolds number is small ( $< 1$ ), the Stokes drag dominates and the droplet terminal velocity ( $\sim v_{\text{gas}}$ ) is expected to be

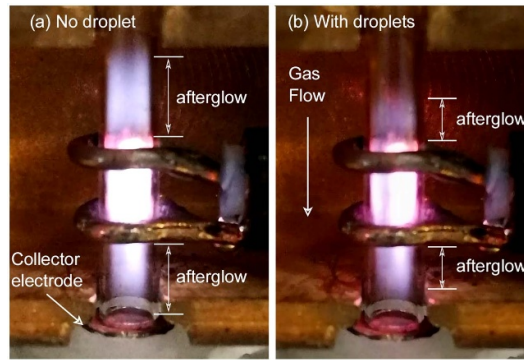


Figure 6. Plasma afterglow—luminous length extends beyond the plasma electrodes.

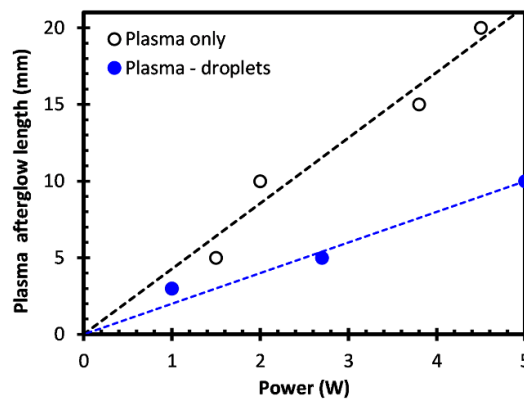


Figure 7. Plasma afterglow length (luminous) versus absorbed power for plasma with and without droplets.

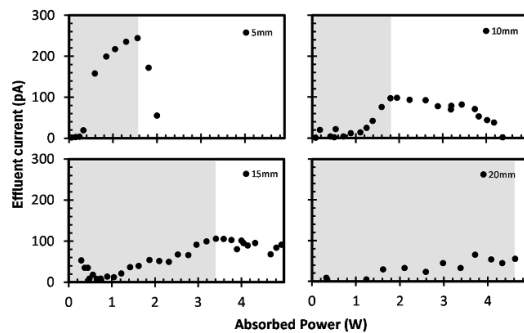
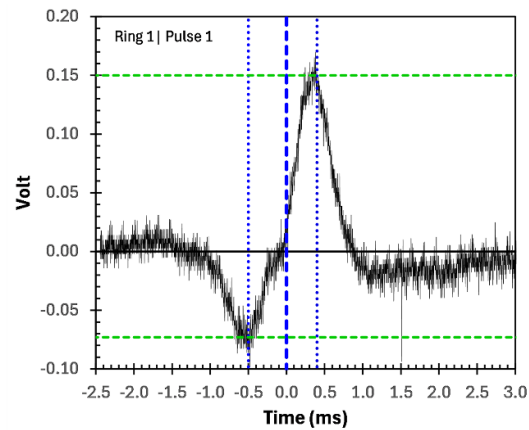
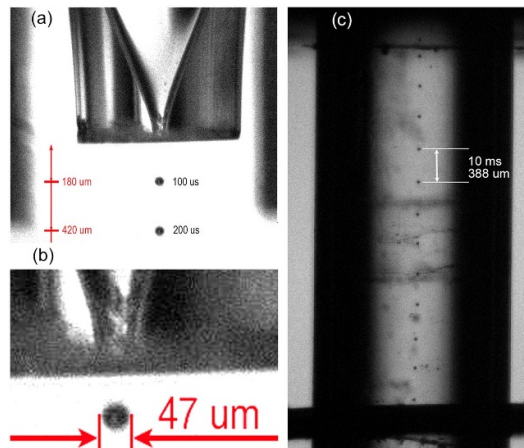


Figure 8. Effluent current versus power indicating the variation in power threshold for coupling to plasma afterglow for various distances between plasma electrode and current measurement electrode. The shaded region, representing the safe power range, is defined conservatively at the estimated point of peak positive current, to ensure the electrode is outside the afterglow region. At 20 mm, no peak is observed and the safe power is given by the maximum absorbed power.

reached within 3 mm of the He gas inlet, which is far upstream ( $\sim 20$  mm) from the plasma and ring. Assuming laminar flow conditions at the ring, i.e. a parabolic velocity profile, the peak velocity at zero offset ( $x = 0$ ) is  $4.2 \text{ ms}^{-1}$ , while for an offset  $x = 0.67a$ , the velocity is  $0.45 \text{ ms}^{-1}$ , equal to the measured droplet velocity. A droplet velocity of  $0.44 \text{ m s}^{-1}$  was also estimated from the time interval between pulses on a second ring located a fixed distance (21 mm) away.



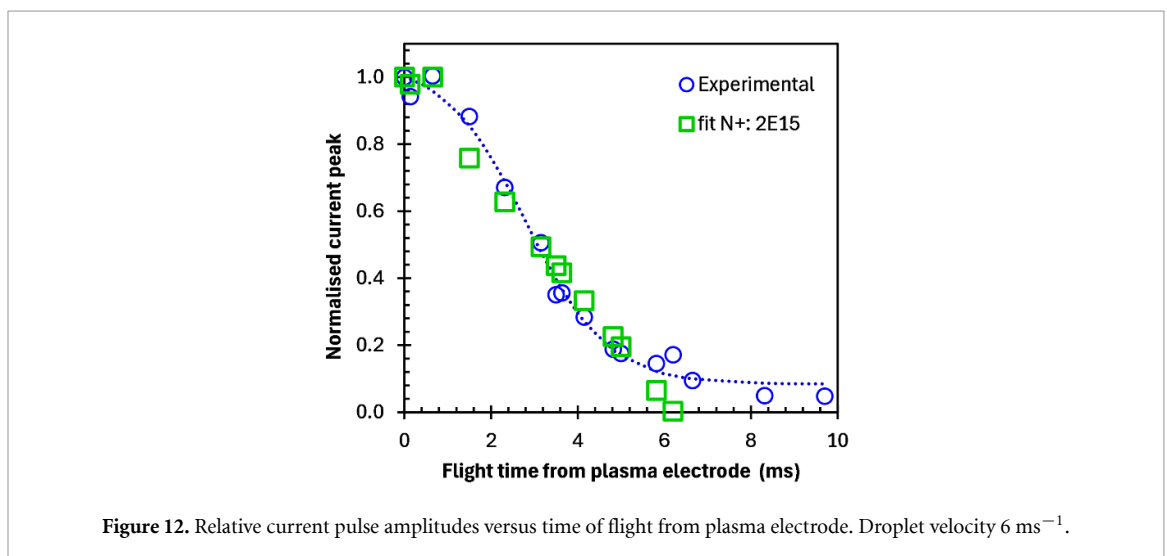
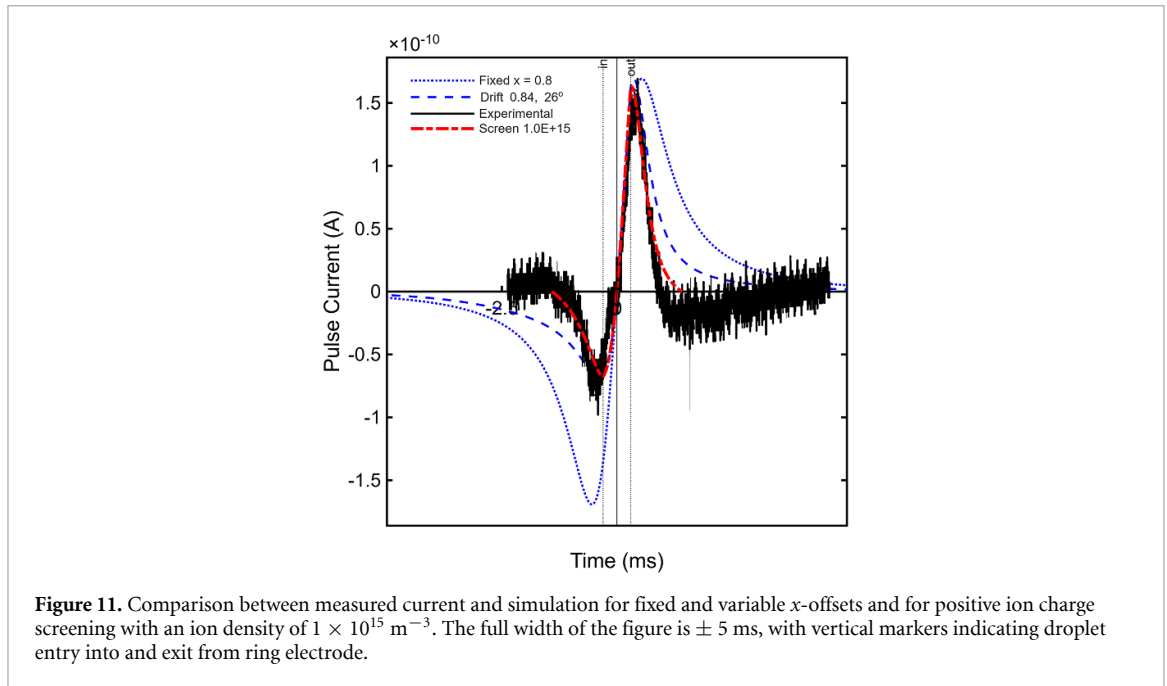
**Figure 9.** Typical ring voltage pulse due to passage of an individual charged microdroplet through the ring. The signal mean has been zeroed to remove a negative DC offset. The pulse width (peak—peak) is  $\sim 1$  ms. Scaling factor:  $1 \text{ V} = 10^{-9} \text{ A}$ . The microdroplet/pulse frequency was 20 Hz. For analysis, signal averaging is carried out using 200 pulse signal acquisitions.



**Figure 10.** Droplet size and velocity determination. (a) Droplets exiting piezo generator tip at a velocity of  $2.1 \text{ m s}^{-1}$  into still air, (b) enlarged image at tip, droplet diameter of  $47 \mu\text{m}$ . Dimensions are calibrated against vernier calliper measurements of the tip enclosure ( $806 \mu\text{m}$ ), (c) droplets (100 Hz) within plasma region, with He flow but without plasma ignited showing  $388 \mu\text{m}$  separation, for a set interval of 10 ms.

Simulated current pulses were generated for a droplet velocity of  $0.45 \text{ m s}^{-1}$  and an  $x$ -offset value of 0.68a, as observed experimentally. Also, since the pulse is asymmetric, this indicates a variation in  $x$ -offset during flight. In figure 11, a comparison between simulated and measured currents is shown. Peak heights are matched using charge values from  $2.5 \times 10^6$  electrons (fixed  $x$ -offset) to  $3.5 \times 10^6$  electrons (variable offset).

The rapid decay in pulse amplitude may be attributed to screening by the background positive ion density, which was adjusted to  $1 \times 10^{15} \text{ m}^{-3}$  to provide an optimal fit to the measured pulse shape. The effect of positive ion density on droplet charge neutralisation was also investigated by comparing pulse amplitudes in two rings, separated by a gap of 21 mm. Over this distance, the observed decay (72%) indicates, from (9), an ion density of  $1.8 \times 10^{14} \text{ m}^{-3}$  and the expected decay between plasma and ring is  $\sim 17\%$ . A similar calculation was carried out for pulses obtained from a high-rate droplet stream (50 kHz) with a single ring electrode positioned at various distances, up to 60 mm, from the capillary output. In this case, the droplet diameters follow a lognormal distribution (mean  $13 \mu\text{m}$ ) with velocities in the range of  $3\text{--}14 \text{ m s}^{-1}$ . Figure 12 shows an example fit to the experimentally observed charge decay for a droplet velocity of  $6 \text{ m s}^{-1}$  and an ion density of  $2 \times 10^{15} \text{ m}^{-3}$ .



## 5. Discussion

The estimated value of charge on fixed size individual droplets varied from  $2.5$  to  $3.5 \times 10^6$  electrons, depending on the  $x$ -offset conditions chosen to match the observed droplet velocity to that of the gas. Due to charge neutralisation by the weak background positive space charge between the end of the plasma and the ring electrode, the measured values are estimated to be  $\sim 17\%$  lower than when droplets are in the plasma region. This is a higher level of charge, by a factor of  $2$ – $3$ , compared to our measurements made previously with smaller droplets using a solid plate electrode downstream of the capillary, and extrapolated to a larger diameter,  $47 \mu\text{m}$ , reported here [23]. The two sets of measurements are not expected to be directly comparable due to variations in plasma conditions for different gas flows, the wider distributions of charge and velocity values in the latter along with possible higher neutralisation and flow effects around a solid measurement electrode situated in air. Previously, finite element simulations were carried out to estimate the acquired charge, assuming a fully collisional plasma and using electron and positive ion drift–diffusion equations to the droplet surface. These were coupled via Poisson’s equation to the floating potential of the charged droplet, which was iterated until the electron and ion flux were equal. The main parameters were  $n_e$ ,  $T_e$ , ion mobility,  $\mu_{\text{ion}}$  and  $R_d$ . For both ring and plate measurement sets, simulations predicted lower levels of charge than observed. In the latter case, reduction of the ion mobility to account for large slow positive cluster ions offers a possible

solution. Such ions are expected due to the layer of saturated water vapour surrounding an evaporating droplet travelling at the same speed as the gas and hence are also likely to be present in the ring measurements. Multiple collisions between  $\text{He}_2^+$  ions and the evaporated water molecules surrounding the droplet lead to the growth of large positive,  $\text{H}^+(\text{H}_2\text{O})_n$ , and negative  $\text{OH}^-(\text{H}_2\text{O})_n$ , water cluster ions, with the cluster size increasing with vapour content [29–31]. Large positive cluster ions with  $n$  up to 55 ( $\sim 1000$  amu) have been reported for a He plasma jet into air [32]. For the estimated average values of  $n_e = 10^{20} \text{ m}^{-3}$  and  $T_e = 2 \text{ eV}$ , the predicted charge from the simulation for  $R_d = 24 \text{ }\mu\text{m}$ , was  $7 \times 10^5$  electrons and  $1.2 \times 10^6$  electrons for ion mobility values of  $2.5 \times 10^{-3} \text{ V m}^{-2} \text{ s}^{-1}$  ( $\text{He}_2^+$ ) and  $1.0 \times 10^{-5} \text{ V m}^{-2} \text{ s}^{-1}$  ( $\text{H}_2\text{O})_n^+$  respectively. Therefore, for ion mobilities dominated by large water cluster ions, the measured charge is 2–3 times that obtained from simulations. However, a further reduction in ion mobility is not realistic.

From a technological perspective, charged droplets may have important applications in, for example, downstream spatial printing of advanced materials. In the case of a higher velocity droplet stream, the neutralisation rate flattens beyond a time-of-flight post plasma of  $\sim 8 \text{ ms}$ , leaving the droplet charge value at  $\sim 10^5$ – $10^6$  electrons, considerably higher than can be achieved by other techniques, e.g. corona or triboelectric charging. In corona discharge systems at atmospheric pressure, ions are primarily responsible for particle charging because high mobility electrons are quickly lost through attachment and recombination in dense gases. Reported values for corona charging range from approximately 100 electrons for  $1 \text{ }\mu\text{m}$  particles to about 2000 electrons for  $7 \text{ }\mu\text{m}$  particles [33]. In dusty plasmas, charging measurements are largely limited to nanoparticles at high pressure and microparticles at low pressure. Simulations suggest nanoparticle charges of around 200 electrons for  $125 \text{ nm}$  diameter particles [24], while low-pressure plasma experiments show values ranging from 10 to  $10^4$  electrons for particles up to  $\sim 10 \text{ }\mu\text{m}$  diameter [33–36].

However, the more significant technological potential may be in the exploitation of plasma charged droplets as chemical microreactors. We have previously shown an enhancement of reaction rates in droplets by many orders of magnitude compared to bulk techniques for Au nanoparticle formation from metal salt reduction and for  $\text{H}_2\text{O}_2$  synthesis [23, 37]. Solvated electron reactions drive the former and are likely an important element of the latter. Therefore, important parameters for microreactors are the electron charge magnitude, charge flux to the surface and plasma time-of-flight. The observed values of charge can be matched in simulations by increasing  $n_e$  and  $T_e$ , typically charge increases by factors of  $x3$  to  $x5$  per decade increase in electron density and similarly for increases in  $T_e$  up to 13 eV. In the simulations we have used time and spatially averaged values of  $n_e$  obtained from impedance measurements which assume a uniform density cylindrical plasma. Without droplets, the calculated electron density was approximately constant with power, up to 3.5 W, at  $3 \times 10^{18} \text{ m}^{-3}$ . In a similar plasma device, using argon,  $n_e$  and  $T_e$  were determined from Stark broadening to be  $>10^{20} \text{ m}^{-3}$  and  $\sim 1 \text{ eV}$  respectively [38]. With the introduction of droplets,  $n_e$  increased linearly with power up to  $10^{20} \text{ m}^{-3}$  at 5 W [23]. While the reason for this is unclear, we observed that since the afterglow regions were reduced with droplets, the estimated input volumetric power density had increased.

In order for the droplet to ‘see’ higher electron densities or temperatures that could account for the measured charge in the simulation, we might speculate that spatiotemporal variations in  $n_e$  and  $T_e$  could be significant, especially near the driven electrode and at the sheath edge where the droplet may come close, given the  $x$ -offset is  $\sim 0.7a$ . Spatial and/or temporal models of RF-driven plasmas at atmospheric pressure are limited and none match the geometrical configuration used here. Various groups have estimated  $n_e(x,t)$  and  $T_e(x,t)$  from measurements and/or simulations for parallel-plate geometries [39–42]. These indicate various possibilities from limited temporal variation in  $n_e$  over a cycle, except near the sheaths [40, 43], to increased  $n_e$  by factors up to  $x10$ , twice per cycle [44] while an increasing ratio of peak  $n_e$  to average was predicted as electrode gap reduced [39]. Similarly, for  $T_e$ , with instantaneous values a factor of  $\sim 3$ – $5$  above the average near sheaths [43, 45]. In such an eventuality, the question is whether the elevated charge acquired in elevated density or temperature regions remains until the droplet exits the plasma or rapidly equilibrates to the local density and temperature. To evaluate this, we consider a droplet charged near the upper electrode (RF-driven) with local excess  $n_e$  and  $T_e$  which then passes through the remainder of the plasma region (2 mm, 4 ms) of uniform  $n_e$  and  $T_e$ , as used in simulations. The charge flux density at the droplet surface is constant at a value of  $10^{20} \text{ m}^{-2} \text{ s}^{-1}$ – $3 \times 10^{22} \text{ m}^{-2} \text{ s}^{-1}$  for low and high mobility values. Assuming, for simplicity, that the electron flux  $\sim 0$  until the charge is equilibrated, then sufficient ion neutralisation would occur within only  $15 \text{ }\mu\text{m}$  of travel. Therefore, spatial variation in  $n_e$  or  $T_e$  leading to elevated charging would effectively be temporary. However, if  $n_e$  and  $T_e$  are spatially uniform but vary with RF amplitude, the required neutralisation

time is  $>100$  times the RF period and hence enhanced plasma charging as a result of temporal spikes in plasma parameters is plausible.

Finally, chemical reaction rate enhancement in charged droplets, via techniques other than plasma exposure, has indicated a strong size and surface area effect, with surface species concentration and electric fields thought to be implicated. We observe from simulations an increase in charge with diameter which follows a second order polynomial fit. However, the flux density decreases with diameter and hence we can expect that chemical reaction rate enhancement, which likely depends on species concentrations in a shallow surface layer, will also be favoured as the diameter is reduced. Furthermore, the surface electric field obtained from droplet charge simulations (COMSOL) also shows a rapid increase for smaller droplets. From a technological perspective, the minimum droplet size will depend on the evaporation rate, which will determine the lifetime of the reactor [20]. With the RF-driven plasma system, we have previously measured evaporation rates approximately ten times higher than those in flowing gas at room temperature. Under these conditions, droplets with initial diameters under  $5\ \mu\text{m}$  are totally evaporated after  $100\ \mu\text{s}$  plasma exposure time. Using the high-rate droplet source, where large reaction rate enhancements were observed, the mean droplet diameter was  $13\ \mu\text{m}$ , and while the current single droplet system can produce droplets as small as  $15\ \mu\text{m}$ , it was found that most droplets smaller than  $\sim 40\ \mu\text{m}$  were lost to the walls at the gas mixer inlet. Future developments will address this issue.

## 6. Conclusions

We have demonstrated single droplets with net negative acquired charges after short exposure to a low temperature RF-driven atmospheric pressure plasma. The measured acquired charge was between  $2.5 \times 10^6$  electrons and  $3.5 \times 10^6$  electrons which is  $\sim 20\%$  of the Rayleigh limit for a  $47\ \mu\text{m}$  diameter water droplet. These values are much higher than those obtained from simulations with helium ions and possible reasons include reduced positive ion mobility due to the creation of large heavy water cluster ions in the evaporation halo around the droplet and temporal enhancement of electron density and temperature with RF amplitude. Overall, the droplet in plasma system is a complex multiphase environment but one that offers exciting opportunities for technological exploitation such as chemical microreactors and advanced materials manufacture.

## Data availability statement

The data cannot be made publicly available upon publication because the cost of preparing, depositing and hosting the data would be prohibitive within the terms of this research project. The data that support the findings of this study are available upon reasonable request from the authors.

## Acknowledgment

This work was supported by Engineering and Physical Sciences Research Council (Project Nos. EP/K006088/1, EP/K006142/1, EP/K022237/1, EP/R008841/1, EP/T016000/1) and EU COST Actions PLAgri (CA19110) and PlasTHER (CA20114).

## ORCID iDs

Nourhan E Hendawy  0000-0002-0248-1341

Harold N McQuaid  0000-0001-8100-6778

Declan Diver  0000-0001-6478-6020

Davide Mariotti  0000-0003-1504-4383

## References

- [1] Wei Z, Li Y, Cooks R G and Yan X 2020 Accelerated reaction kinetics in microdroplets: overview and recent developments *Annu. Rev. Phys. Chem.* **71** 31–51
- [2] LaCour R A, Heindel J P, Zhao R and Head-Gordon T 2025 The role of interfaces and charge for chemical reactivity in microdroplets *J. Am. Chem. Soc.* **147** 6299–317
- [3] Chen H, Li X, Li B, Chen Y, Ouyang H, Li Y and Zhang X 2025 Microdroplet chemistry with unactivated droplets *J. Am. Chem. Soc.* **147** 11399–406
- [4] Meng Y, Xia Y, Xu J and Zare R N 2025 Spraying of water microdroplets forms luminescence and causes chemical reactions in surrounding gas *Sci. Adv.* **11** 8979

- [5] Bose S, Mofidfar M, Zare R N and Gnanamani E 2025 Cross-coupling between arylboronic acids and terminal alkynes in water microdroplets *J. Am. Chem. Soc.* **147** 25779–86
- [6] Meng Y, Gnanamani E and Zare R N 2023 One-step formation of pharmaceuticals having a phenylacetic acid core using water microdroplets *J. Am. Chem. Soc.* **145** 7724–8
- [7] Chamberlayne C F and Zare R N 2020 Simple model for the electric field and spatial distribution of ions in a microdroplet *J. Chem. Phys.* **152** 184702
- [8] Lin S, Cao L N Y, Tang Z and Wang Z L 2023 Size-dependent charge transfer between water microdroplets *Proc. Natl Acad. Sci. USA* **120** e2307977120
- [9] Jia X, Wu J and Wang F 2024 Water-microdroplet-driven interface-charged chemistries *J. Am. Chem. Soc.* **4** 4141–7
- [10] Song X, Basheer C and Zare R N 2023 Making ammonia from nitrogen and water microdroplets *Proc. Natl Acad. Sci. USA* **120** e2301206120
- [11] Bose S, Mofidfar M and Zare R N 2024 Direct conversion of N<sub>2</sub> and air to nitric acid in gas-water microbubbles *J. Am. Chem. Soc.* **146** 27964–71
- [12] Mehrgardi M A, Mofidfar M, Li J, Chamberlayne C F, Lynch S R and Zare R N 2024 Catalyst-free transformation of carbon dioxide to small organic compounds in water microdroplets nebulized by different gases *Adv. Sci.* **11** 2406785
- [13] Meng Y, Gnanamani E and Zare R N 2025 Water droplet microlightning sparks alkyne ozonolysis *J. Am. Chem. Soc.* **147** 23399–404
- [14] Lee J K, Samanta D, Nam H G and Zare R N 2019 Micrometer-sized water droplets induce spontaneous reduction *J. Am. Chem. Soc.* **141** 10585–9
- [15] Mehrgardi M A, Mofidfar M and Zare R N 2022 Sprayed water microdroplets are able to generate hydrogen peroxide spontaneously *J. Am. Chem. Soc.* **144** 7606–9
- [16] Mofidfar M, Mehrgardi M A, Xia Y and Zare R N 2024 Dependence on relative humidity in the formation of reactive oxygen species in water droplets *Proc. Natl Acad. Sci. USA* **121** e2315940121
- [17] Zhou J, Wang Q, Cheng G, Shen W, Zare R N and Sun X 2025 Charged water microdroplets enable dissociation of surrounding dioxygen *J. Am. Chem. Soc.* **147** 10916–24
- [18] Xia Y, Xu J, Li J, Chen B, Dai Y and Zare R N 2024 Visualization of the charging of water droplets sprayed into air *J. Phys. Chem. A* **128** 5684–90
- [19] Kumar A, Avadhani V S, Nandy A, Mondal S, Pathak B, Pavuluri V K N, Avulapati M M and Banerjee S 2024 Water microdroplets in air: a hitherto unnoticed natural source of nitrogen oxides *Anal. Chem.* **96** 10515–23
- [20] Bennet E D et al 2016 Precision charging of microparticles in plasma via the Rayleigh instability for evaporating charged liquid droplets *J. Aerosol. Sci.* **100** 53–60
- [21] Hendawy N, McQuaid H, Mariotti D and Maguire P 2020 Continuous gas temperature measurement of cold plasma jets containing microdroplets, using a focussed spot IR sensor *Plasma Sources Sci. Technol.* **29** 085010
- [22] Maguire P D et al 2015 Controlled microdroplet transport in an atmospheric pressure microplasma *Appl. Phys. Lett.* **106** 224101
- [23] Hendawy N, McQuaid H, Uidhir S M, Rutherford D, Diver D, Mariotti D and Maguire P 2025 Free electron charging of microdroplets in a plasma at atmospheric pressure (arXiv:2508.13372)
- [24] Abuyazid N H, Chen X, Mariotti D, Maguire P, Hogan C J and Sankaran R M 2020 Understanding the depletion of electrons in dusty plasmas at atmospheric pressure *Plasma Sources Sci. Technol.* **29** 075011
- [25] He Z 2001 Review of the Shockley–Ramo theorem and its application in semiconductor gamma-ray detectors *Nucl. Instrum. Methods Phys. Res. A* **463** 250–67
- [26] Ramo S 1939 Currents induced by electron motion *Proc. IRE* **27** 584–5
- [27] Shockley W 1938 Currents to conductors induced by a moving point charge *J. Appl. Phys.* **9** 635–6
- [28] Kucerovsky Z and Greason W D 2007 Attrition of the charge on a carrier moving through a gas *IEEE Trans. Ind. Appl.* **43** 1515–23
- [29] Große-Kreul S, Hübner S, Schneider S, Ellerweg D, Von Keudell A, Matejčík S and Benedikt J 2015 Mass spectrometry of atmospheric pressure plasmas *Plasma Sources Sci. Technol.* **24** 044008
- [30] Tavant A and Lieberman M A 2016 Hybrid global model of water cluster ions in atmospheric pressure Ar/H<sub>2</sub>O RF capacitive discharges *J. Phys. D: Appl. Phys.* **49** 465201
- [31] Abd-Allah Z, Sawtell D A G, McKay K, West G T, Kelly P J and Bradley J W 2015 Mass spectrometric investigation of the ionic species in a dielectric barrier discharge operating in helium-water vapour mixtures *J. Phys. D: Appl. Phys.* **48** 085202
- [32] McKay K, Oh J-S, Walsh J L and Bradley J W 2013 Mass spectrometric diagnosis of an atmospheric pressure helium microplasma jet *J. Phys. D: Appl. Phys.* **46** 464018
- [33] Kersten H, Deutsch H and Kroesen G M W 2004 Charging of micro-particles in plasma–dust interaction *Int. J. Mass Spectrom.* **233** 51–60
- [34] Mendis D A 2002 Progress in the study of dusty plasmas *Plasma Sources Sci. Technol.* **11** A219
- [35] Trottenberg T, Melzer A and Piel A 1995 Measurement of the electric charge on particulates forming Coulomb crystals in the sheath of a radiofrequency plasma *Plasma Sources Sci. Technol.* **4** 450–8
- [36] Beckers J, Ockenga T, Wolter M, Stoffels W W, Van Dijk J, Kersten H and Kroesen G M W 2011 Microparticles in a collisional rf plasma sheath under hypergravity conditions as probes for the electric field strength and the particle charge *Phys. Rev. Lett.* **106** 115002
- [37] Maguire P, Rutherford D, Macias-Montero M, Mahony C, Kelsey C, Tweedie M, Pérez-Martin F, McQuaid H, Diver D and Mariotti D 2017 Continuous in-flight synthesis for on-demand delivery of ligand-free colloidal gold nanoparticles *Nano Lett.* **17** 1336–43
- [38] Askari S, Levchenko I, Ostrikov K, Maguire P and Mariotti D 2014 Crystalline Si nanoparticles below crystallization threshold: effects of collisional heating in non-thermal atmospheric-pressure microplasmas *Appl. Phys. Lett.* **104** 163103
- [39] Liu D X, Yang A J, Wang X H, Rong M Z, Iza F and Kong M G 2012 Wall fluxes of reactive oxygen species of an rf atmospheric-pressure plasma and their dependence on sheath dynamics *J. Phys. D: Appl. Phys.* **45** 305205
- [40] Liu H et al 2021 Electron heating mode transitions in radio-frequency driven micro atmospheric pressure plasma jets in He/O<sub>2</sub>: a fluid dynamics approach *J. Appl. Phys.* **54** 275204
- [41] Nayak G, Meyer M, Oinuma G, Kushner M J and Bruggeman P J 2023 The transport dynamics of tens of micrometer-sized water droplets in RF atmospheric pressure glow discharges *Plasma Sources Sci. Technol.* **32** 045005

- [42] Yang A, Liu D, Rong M, Wang X and Kong M G 2014 A dominant role of oxygen additive on cold atmospheric-pressure He + O<sub>2</sub> plasmas *Phys. Plasmas* **21** 083501
- [43] Liu Y, Liu D, Zhang J, Sun B, Yang A and Kong M G 2020 1D fluid model of RF-excited cold atmospheric plasmas in helium with air gas impurities *Phys. Plasmas* **27** 043512
- [44] Klich M, Wilczek S, Donkó Z and Brinkmann R P 2022 Simulation and modeling of radio-frequency atmospheric pressure plasmas in the non-neutral regime *Plasma Sources Sci. Technol.* **31** 045003
- [45] Klich M, Schulenberg D, Wilczek S, Vass M, Bolles T, Korolov I, Schulze J, Mussenbrock T and Brinkmann R P 2025 Electron dynamics of three distinct discharge modes of a cross-field atmospheric pressure plasma jet *Plasma Sources Sci. Technol.* **34** 045012